Supplemental Figures and Legends

A

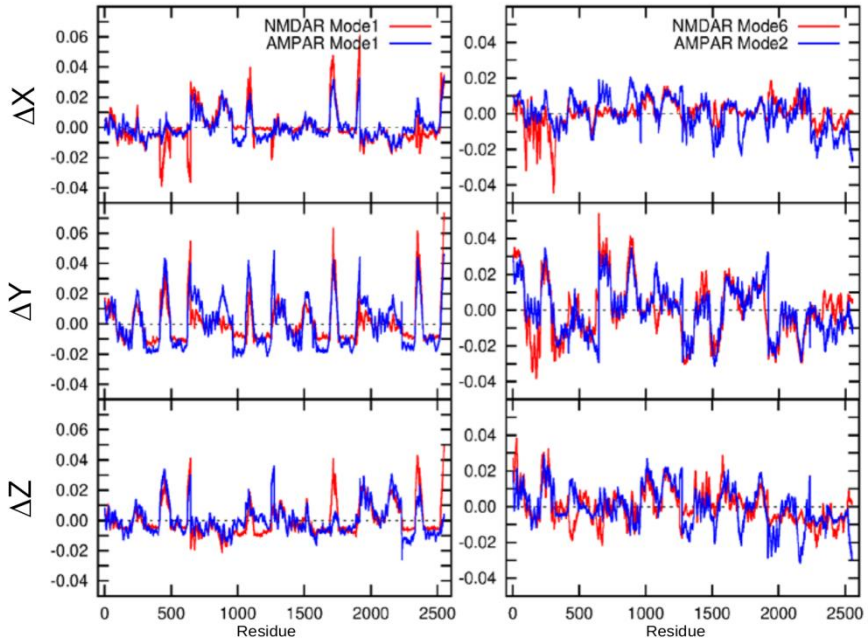

B

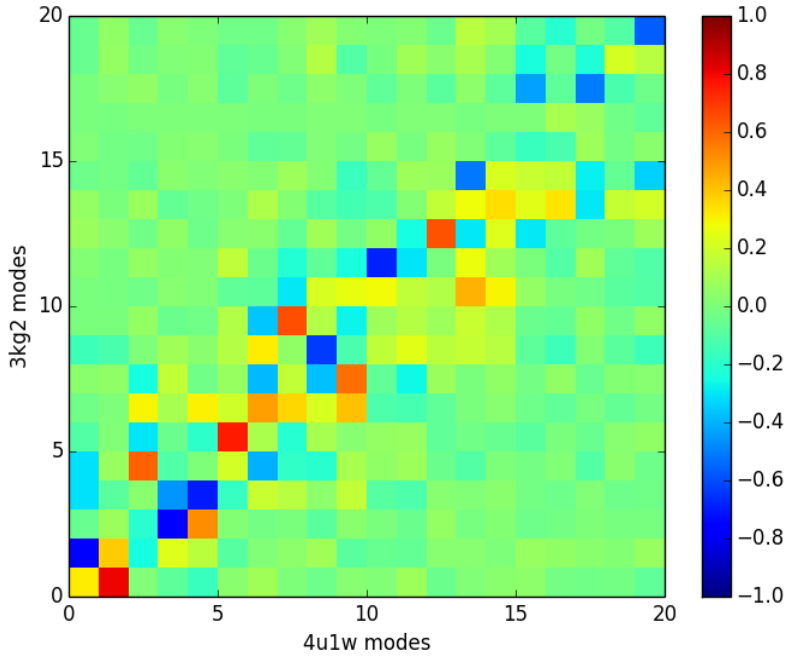

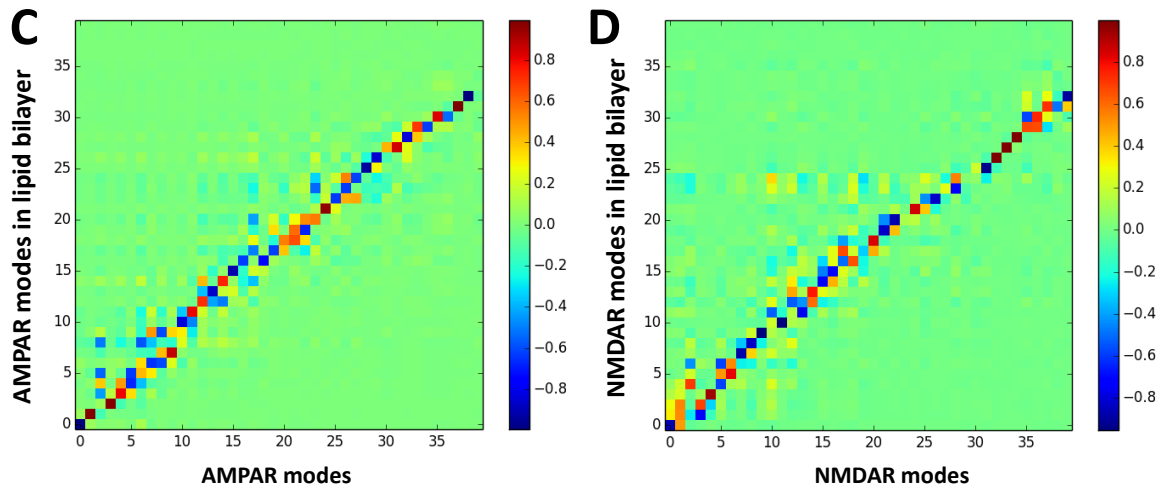

Figure S1, related to Figure 1. Further comparison of AMPAR and NMDAR global modes. (A) The X-, Y-, and Z- directions of some comparable AMPAR and NMDAR modes is shown to illustrate the high degree of overlap between them. The left panels compare *mode 1* of the AMPAR core (PDB id: 3KG2) (Sobolevsky et al., 2009) and that of the NMDAR (PDB id: 4PE5) (Karakas et al., 2014). The correlation cosine between these two modes is 0.77 (see *Movie 1*). The curves are directly obtained from the *3N*-dimensional eigenvectors $\boldsymbol{u}_{c1}^{\text{AMPAR}}$ and $\boldsymbol{u}_{c1}^{\text{NMDAR}}$ that are uniquely defined by the inter-residue contact topology of the respective structures (see Supplemental Methods). The right panels display similar results for the pair of modes $\boldsymbol{u}_{c2}^{\text{AMPAR}}$ and $\boldsymbol{u}_{c6}^{\text{NMDAR}}$. The corresponding correlation cosine is 0.67 (see *Movie 4*). Similar calculations (not shown) for the pair ($\boldsymbol{u}_{c3}^{\text{AMPAR}}$, $\boldsymbol{u}_{3}^{\text{NMDAR}}$) yielded a correlation cosine of 0.67 (*Movie 5*); and $\cos(\mathbf{u}_{c5}^{\text{AMPAR}}, \mathbf{u}_{c2}^{\text{NMDAR}}) = 0.63$. Note that these observed correlations are enhanced by a factor of 60-70 compared to random, in support of the tendency of the two iGluRs to share similar mechanisms of global rearrangements. **(B)** The first 20 global modes of AMPAR structures are similar to those of the first whole AMPAR crystal structure (PDB id: 3KG2) (Sobolevsky et al., 2009). A comparison to a structure with kainate and the LBD modulator (R,R)-2b (PDB id: 4U1W) (Durr et al., 2014) is shown as an example. (**C**) and (**D**) Comparison of the soft modes obtained in the presence of the lipid bilayer (*ordinate*) with those obtained in the absence of the lipid bilayer (*ordinate*), shown for the intact AMPAR (**C**) and NMDAR (**D**) structures. A strong overlap between the two mode spectra is observed for each iGluR, indicating that the global dynamics of either receptor is relatively insensitive to the perturbations exerted by the membrane environment. The most strongly affected mode in both cases appears to be mode 3, which corresponds to a global torsional rotation of the TMD. The presence of the membrane appears to restrict (if not eliminate) this mode which is now replaced by a combination of relatively higher frequency (stiffer) modes.

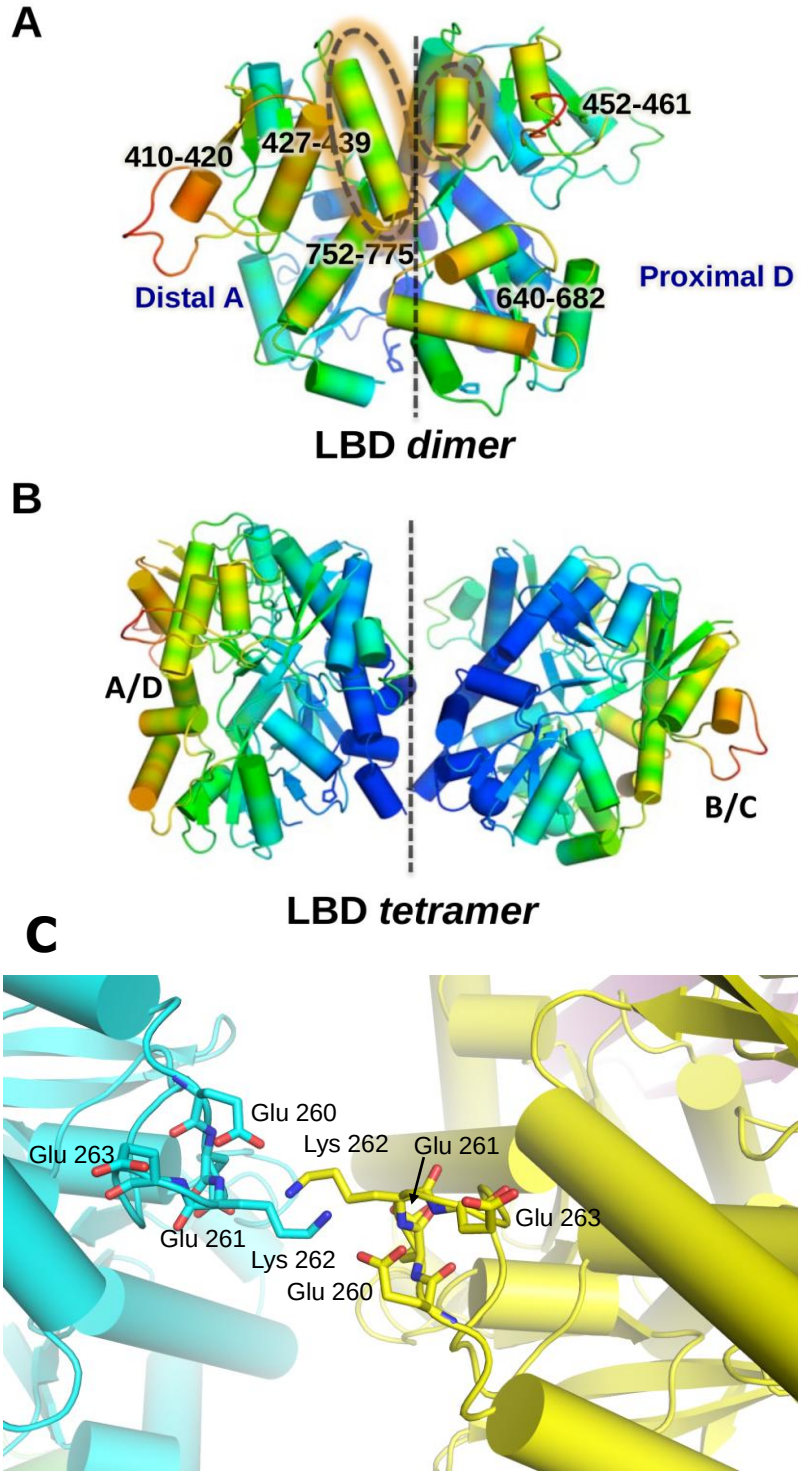

Figure S2, related to Figure 4. Characteristic motions in the AMPAR LBD captured by u_2^{AMPAR} (A-B): The differences in the mobility of the LBD proximal and distal chains (highlighted in **Figure 4C**) are described here by a color-coded (from *red* (most mobile) to *blue* (most rigid)) diagram of the LBD. In the LBD dimer (**A**), the helix comprising residues 742-757 forms interfacial contacts with residues 482-495 that form a helix-loop region; these are helices circled. Regions of the LBD distal and proximal chains that show high mobility are numbered. **B** shows the side view of the whole

receptor LBD, where we see that the *A/D* dimer shares a tetramer interface with the *B/C* dimer. This tetramer interface between subunits results in dampening of the motions at this otherwise symmetric end of the LBD dimer (distal-proximal pair). Thus the symmetric intradimer interface formed now by residues 742-757 of proximal chain *D* and residues 482-495 of distal chain *A*, show less mobility than their respective counterparts in **A** with regions numbered in **A** showing dampened motion. This accounts for the difference in mobilities highlighted in **Figure 4C**. **(C)** The region surrounding K262 contains many negatively charged residues that could accommodate the positive charges of K262 amine groups. The panel shows these residues in our high resolution GluA2 NTD structure (PDB: 3HSY; Rossmann et al. *EMBOJ* 2011), aligned onto the ANM mode 2 'closed' state.

Supplemental Movies

Supplemental Movies can be accessed in the attachment (11 movies, named Movie 1-Movie 11). They can also be viewed on the web, at

http://csb.pitt.edu/bahar/NMDAR_vs_AMPAR.html

The movies are organized as:

Movies 1-8. We present here the animations of selected collective modes intrinsically accessible to the two iGluRs (see Figure 1B). The movies are organized in pairs to allow for direct comparison of equivalent (similar) global modes between AMPAR (PDB id: 3KG2) and NMDAR (PDB id: 4PE5). Most movies are color-coded from *blue* (most rigid) to *red* (most mobile), except for a few cases colored by chain (subunit A: *green*; B: *blue*, C: *magenta*; D: *yellow*) for better visualization of the relative movements of the individual subunits. Below is the list of movies generated for either the full length receptors or the core structures.

Movie 1. Comparison of AMPAR *mode 1* and NMDAR *mode 1* for the full length (A-B) and core (C-D) structures.
Movie 2. Comparison of full length AMPAR *mode 3* and full length NMDAR *mode 4*.
Movie 3. Comparison of full length AMPAR *mode 7* and full length NMDAR *mode 6*.
Movie 4. Comparison of AMPAR core *mode 2* and NMDAR core *mode 6*.
Movie 5. Comparison of AMPAR core *mode 3* and NMDAR core *mode 3*.
Movie 6. Comparison of AMPAR core *mode 4* and NMDAR core *mode 4*.
Movie 7. Comparison of AMPAR core *mode 7* and NMDAR core *mode 7* (A-B) and AMPAR core *mode 10* and NMDAR core *mode 8* (C-D).
Movie 8. Comparison of AMPAR core *mode 14* and NMDAR core *mode 12*.

Movie 9. ANM *mode 6* accessible to AMPAR core, which plays a major role in the interconversion from the crystallographically resolved AMPAR structure (PDB id: 3KG2) toward the NMDAR structure (PDB id: 4PE5) (see Figure 1C).

Movie 10. ANM *mode 4* accessible to full length AMPAR (counterpart of core *mode 6*; movie 9), which plays a major role in the interconversion from the crystallographically resolved AMPAR structure (PDB id: 3KG2) toward the NMDAR structure (PDB id: 4PE5) (see Figure 3).

Movie 11. Coupling between NTD inter-dimer opening/closing and LBD-NTD packing, shown for ANM core *mode 17* accessible to NMDAR. This mode makes the largest contribution to the

reconfiguration of the crystallographically resolved NMDAR structure (PDB id: 4PE5) toward the AMPAR structure (PDB id: 3KG2) (see Figure 1D).

Supplemental Methods

Analysis of Collective Modes using the Elastic Network Models ANM and GNM

In the ANM the protein is represented as a network where residues serve as the nodes, the positions of which are identified by those of α-carbons, and the overall potential is represented as the sum of harmonic potentials between interacting nodes (C^{α}-C^{α} < 15Å) (Atilgan et al., 2001). The force constants for the *3N* x *3N* interactions (for *N* residues in *3D*) are given by the elements of the Hessian matrix **H**. The inverse $\mathbf{H}^{-1}$ is proportional to the covariance of residue fluctuations away from their mean position (**C**).

To achieve a conformation displaced along one of the ANM modes, we use the following equation: $\mathbf{R}^{(k)} = \mathbf{R}^{(0)} \pm s\lambda_k^{-1/2}\mathbf{u}_k$, where $\mathbf{R}^0$ is a *3N*-dimensional vector representing initial coordinates. Using different values of *s* we can generate an ensemble of conformations ($\mathbf{R}^{(k)}$) along mode *k*. *s* scales with k_BT/γ, where k_B is the Boltzmann constant, T is temperature and γ is the spring constant. γ can be approximated to reproduce experimental fluctuations from B factors with $B_i = (8\pi^2 k_BT\, tr[\mathbf{H}^{-1}]_{ii}) / 3\gamma$.

The GNM is another ENM where the network nodes (C^{α} atoms) are assumed to undergo *isotropic* and *Gaussian* fluctuations about their mean positions (Bahar et al., 1997). The *N x N* Kirchhoff matrix **Γ** replaces **H**, with elements given by $\mathbf{\Gamma}_{ij} = -1$ if $R_{ij} < R_{cut}$ and 0 otherwise, and $\mathbf{\Gamma}_{ii} = -\Sigma_{j,\, j\neq i}\, \mathbf{\Gamma}_{ij}$, where R_{ij} is the magnitude of the distance vector between nodes *i* and *j* and R_{cut} = 7.5 Å. Eigenvalue decomposition of **Γ** yields the frequencies/eigenvalues (σ_k) and shapes/eigenvectors ($\boldsymbol{v}_k$) of the *N-1* GNM modes ($1 \le k \le N$), which in turn may be used for evaluating the cross-correlation matrix $\mathbf{C}_{GNM} = \mathbf{\Gamma}^{-1} = \Sigma_k [\sigma_k^{-1} \boldsymbol{v}_k \boldsymbol{v}_k^T]$ or the *displacement profiles* of residues in the individual modes (simply by plotting the elements of $\boldsymbol{v}_k$; e.g. **Figure 8B** for *k = 2*, plotted for AMPAR (*top*) and NMDAR (*bottom*). Crossover regions (from positive to negative or vice versa) in the displacement profiles of global modes define the hinge sites in those particular modes (e.g. E391 in AMPAR). The other end of the GNM spectrum (the highest frequency/energy modes) defines the centers of energy localization, also called hot spots. The average mobility of a given residue *i* over a subset *S* of high frequency modes is calculated by the weighted average $|\langle M_i \rangle|_S = (\Sigma_k\, \sigma_k^{-1}\, [\boldsymbol{v}_k\, \boldsymbol{v}_k^T]_{ii}) / \Sigma_k\, \sigma_k^{-1}$ where the summations are performed over all modes *k* in the subset *S*. Peaks in $|\langle M_i \rangle|_S$ indicate the residues subject to highest frequency/energy fluctuations, also termed kinetic hotspots (Bahar et al., 1997;Bahar, 2010) (see **Figure 8C**).

Correlation between NMDAR and AMPAR global modes

The correlation between the i^{th} ANM mode of the AMPAR, $\boldsymbol{u}_i^{AMPAR}$, and the j^{th} mode of the NMDAR, $\boldsymbol{u}_j^{NMDAR}$, is evaluated from the correlation cosine between these two *3N*-dimensional eigenvectors, $\cos(\boldsymbol{u}_i^{AMPAR}, \boldsymbol{u}_j^{NMDAR}) = (\boldsymbol{u}_i^{AMPAR} \cdot \boldsymbol{u}_j^{NMDAR})$ where '**.**' designates the dot product (note that the eigenvectors are normalized, hence the omission of the division by their magnitudes). The map in **Figure 1B** is evaluated for all NMDAR and AMPAR modes in $1 \le i, j \le 40$. In the GNM, the

eigenvectors are simply replaced by the N-dimensional eigenvectors obtained by the GNM, $\boldsymbol{v}_i^{\mathrm{AMPAR}}$ and $\boldsymbol{v}_j^{\mathrm{NMDAR}}$ (**Figure 8A**).

The evaluation of the overlap requires the two eigenvectors to have the same dimension. AMPAR and NMDAR have different chain lengths and the different subunits have different missing residues. So, we aligned the structures of the two iGluRs to end up with a 'core' sequence of length N(core) = 2,550 composed of 645, 629, 643 and 633 residues in the respective subunits *A, B, C* and *D* of the receptors Note that the crystallographically resolved structures contained N(AMPAR) = 3,116 and N(NMDAR) = 2,944 residues (respective PDB files of 3kg2 and 4pe5).

The computation protocol consists of the following steps: (i) Structurally align each chain of AMPAR with individual chains of NMDAR. We used to this aim the *"super"* command from Pymol, one chain at a time. (ii) For each chain only keep those residues in AMPAR that have an aligned counterpart in NMDAR. This is for better mapping of residues from one structure to the other, (iii) Superimpose the overall structure of NMDAR to that of AMPAR (or vice versa). Use the mapping of residues obtained from the above steps to calculate a deformation vector $\boldsymbol{d}^{\mathrm{AMPAR}\leftrightarrow\mathrm{NMDAR}}$ (see below), (iv) Perform ANM and GNM analyses on AMPAR and on NMDAR (using only the core structures composed of the mapped residues). (v) Obtain the overlap between ANM modes of AMPAR and NMDAR (**Figure 1B**) and the overlap between the GNM modes of AMPAR and NMDAR (**Figure 8A**), and (vi) obtain the overlap between each the deformation vector and each ANM mode evaluated for AMPAR (**Figure 1C**) ad for NMDAR (**Figure 1D**).

Note that the set of *3N-6* modes form a complete basis set for all possible internal deformations of the *3N*-dimensional structure. As such, the *average* correlation cosine between a given *3N-6* dimensional (unit) vector and an eigenvector is $(1/3N\text{-}6)^{1/2}$, which is 0.0114 for N = 2,550. An observed correlation of 0.5 for example, represents an enhancement over random by a factor of 43.7. Several mode pairs exhibit such strong correlations, as can be viewed on the web.

NMA of a subsystem and its coupling to the environment

In certain cases, we want to probe the behavior of a relevant part of the protein, referred to as the subsystem (ss) and how it responds in the presence of an environment (ee). In the context of a C^{α}-only elastic network model of the protein, we partition the Hessian of the whole system $\mathbf{H}$ into four submatrices (Ming et al., 2006;Zheng et al., 2005)

$$\mathbf{H} = \begin{pmatrix} \mathbf{H}_{SS} & \mathbf{H}_{SE} \\ \mathbf{H}_{ES} & \mathbf{H}_{EE} \end{pmatrix}$$

where $\mathbf{H}_{SS}$ is the Hessian submatrix for the subsystem, $\mathbf{H}_{EE}$ is that of the environment and $\mathbf{H}_{SE}$ (or $\mathbf{H}_{ES}$) indicates coupling between the subsystem and the environment. We assume that the environment minimizes the total energy in response to the subsystems' structural perturbations and obtain an effective Hessian of the subsystem from $\mathbf{H}_{SS}^{(\mathrm{eff})} = \mathbf{H}_{SS} - \mathbf{H}_{SE}\,\mathbf{H}_{EE}^{-1}\,\mathbf{H}_{ES}$. Decomposition of $\mathbf{H}_{SS}^{(\mathrm{eff})}$ gives us the normal modes of the relevant subsystem encompassing the effects of the environment. Decomposition of $\mathbf{H}_{SS}$ gives us the normal modes of the relevant subsystem alone. The correlation between the modes from $\mathbf{H}_{SS}$ and $\mathbf{H}_{SS}^{(\mathrm{eff})}$ is used to quantify the effects of the environment on the subsystem.

ANM analysis of the receptors in the presence of lipid bilayer

In order to check the membrane effects on proteins, we performed ANM analyses for AMPAR and NMDAR in the presence of explicit membrane molecules. The membrane was modeled as a network using the API ProDy (Bakan et al., 2014), as described in a previous study (Lezon et al., 2012). The membrane positions were taken from OPM data base (Lomize et al., 2006). The mode spectrum of the protein (subsystem) in the presence of the membrane (environment) was evaluated as described in the preceding subsection.

Correlation between ANM Modes and Experimental Structural Deformations

The presence of multiple structures (say $\boldsymbol{q}_a$, $\boldsymbol{q}_b$) enables us to assess the capability of ANM modes to predict the transition between these states. To identify how well this targeted deformation ($\boldsymbol{d} = \boldsymbol{q}_b - \boldsymbol{q}_a$) can be achieved by moving along ANM modes, we evaluate the overlap or correlation cosine (I_k) between the eigenvector $\boldsymbol{u}_k$ and $\boldsymbol{d}$, given by $I_k = \boldsymbol{d} \cdot \boldsymbol{u}_k / |\boldsymbol{d}|$. The bars in **Figures 1C** and **1D** represent these correlation cosines obtained for $\boldsymbol{d} = \boldsymbol{d}^{\mathrm{AMPAR} \leftrightarrow \mathrm{NMDAR}}$.

The cumulative overlap (*red curve* in **Figures 1C** and **1D**) contributed by a subset of k modes is given by the square root of the sum of square overlaps over these modes, $[\Sigma_k \, I_k^2]^{1/2}$. Note that again, in the case of a 'random' mode, the overlap would be $(1/3N\text{-}6)^{1/2}$. The green curve illustrates this type of 'expected' correlation if the calculated modes did not correlate with $\boldsymbol{d}$. The large difference between the red and green curve shows that the energetically favored (softest) modes of motion encoded by the NMDAR and AMPAR structures can enable the interconversion between the two resolved structures.

Perturbation Response Scanning (PRS)

This technique measures the response of residues to perturbation at other residues (Atilgan et al., 2009). Briefly, the PRS theory derives from Hooke's law, where the displacement $\Delta\mathbf{r}$ scales linearly with the force, $\mathbf{F} = k\,\Delta\mathbf{r}$, where k is the force constant. In the ANM, the Hessian ($\mathbf{H}$) represents the force constant for the system, i.e. $\mathbf{F} = \mathbf{H}\,\Delta\mathbf{R}$, and consequently $\Delta\mathbf{R} = \mathbf{H}^{-1}\mathbf{F}$. The PRS yields a quantitative measure for the displacement $\Delta\mathbf{R}$ of all residues in response to perturbations $\mathbf{F}_j$ exerted on residue j. The square displacements in response to all scanned residues, $1 \le j \le N$, normalized with respect to the intrinsic mobilities of the responding residues defines the PRS map. To this aim, we evaluate the displacement, $\Delta\mathbf{R}^{(i)}$ of residue i as a result of perturbation, modeled as force applied to residue j. This is called a scanning technique since at any one time we apply force on one residue $\mathbf{F}^{(j)} = [0,0,0, \ldots F_{xj}, F_{yj}, F_{zj}, \ldots 0,0,0]^T$ and repeat for all residues. For each residue j being perturbed, we measure the displacement of the other (N) residues in the x, y and z directions, which is expressed as the $3N$-dimensional vector $\Delta\mathbf{R}$.

Application of the PRS technique to all N residues gives us the elements of the $N \times N$ PRS matrix (**Figure 6A**) where the ij^{th} element gives the displacement of residue j as a result of perturbation at residue i with unit forces averaged over k iterations. We further normalize the ij^{th} element of the PRS matrix by dividing each row by the diagonal element. The PRS matrix is asymmetric: the rows give us the profile of "the effectiveness" of perturbation at residues and the columns give us the profile of "sensitivity" to perturbation. Averaging over rows/columns helps identify residues that act as sensors/effectors (General IJ et al., 2014).

All-Atom Molecular Dynamics Simulations

All steps were carried out using GROMACS 4.6 (Pronk et al., 2013) and the CHARMM27 forcefield (Bjelkmar et al., 2010). Bonds between heavy atoms and hydrogen atoms are constrained with LINCS (Berk et al., 1997), allowing 2 fs time steps. The starting structure was an isolated NTD tetramer (PDB: 3H5V) (Jin et al., 2009), which was imbedded in a rectangular box extending at least 9 Å away from the protein in any direction. This was filled with TIP3P water molecules (Jorgensen et al., 1983), which were then randomly replaced with sodium and chloride ions to neutralize the system and reach a concentration of 70 mM (a total of 230 sodium and 222 chloride ions). Two rounds of steepest descent energy minimization (5000 steps), NVT equilibration (1 ns) and NPT equilibration (1 ns) were performed before production MD. The first round included restraints on the protein heavy atoms to equilibrate the solvent around the protein. The temperature was set at 300 K with the stochastic velocity rescaling thermostat (Bussi et al., 2007) throughout. The pressure was set at 1 bar using the Berendsen barostat during equilibration and the Parrinello-Rahman during production MD. Short-range non-covalent interactions were cutoff at 12 Å using the particle-mesh Ewald method for long-range electrostatics and van der Waals interactions were smoothly switched off between 10 Å and 12 Å. This protocol was carried out for two independent replica each lasting 100 ns.

Crosslinking and surface biotinylation

Mutagenesis was carried out on both full length GluA2 (flip; edited at the R/G site (position 743); unedited at the Q/R site (position 586)) and a Δ-link construct with a modified LBD-NTD linker similar to the $GluA2_{cryst}$ construct used to yield the crystal structure with PDB code 3KG2. The Quikchange Mutagenesis Kit was used to produce the mutants K262C, T44C and S729C. Transfection was carried out in HEK293S cells using the Effectene® transfection reagent (Qiagen) following the manufacturer instructions. Expression was allowed for ~ 36 h at 37 °C and 5 % CO_2, after which surface receptors were biotinylated using EZ-link™ Sulpho-NHS-SS-Biotin (Thermo Scientific) by applying 0.5 mg/ml in PBS for 10 min at 4 °C. Cells were harvested in PBS with protease inhibitors (Roche) and receptors solubilised with lysis buffer (25mM HEPES 7.5, 150mM NaCl, 0.1% SDS, 1% Triton, 1% EDTA and 50 mM NEM) for 30 min at 4 °C. Purification of cell surface receptors was achieved by centrifuging the lysed cells and incubating supernatants with streptavidin beads for 1 h at 4 °C, after which, 3 washes with lysis buffer were done. The result was loaded onto 3-8 % SDS-PAGE gels for western blot analysis. Western blot nitrocellulose membranes were blocked with 5% BSA, incubated with anti-GluA2 C-terminal primary antibody (Sigma) followed by stabilised peroxidase goat anti-rabbit secondary antibody (Thermo Scientific). Membrane development was done with the Supersignal West Dura reagents (Thermo Scientific).

Supplemental References

Bakan,A., Dutta,A., Mao,W.Z., Liu,Y., Chennubhotla,C., Lezon,T.R., and Bahar,I. (2014). Evol and ProDy for bridging protein sequence evolution and structural dynamics. Bioinformatics 30**,** 2681-2683.

Berk,H., Bekker,H., and Herman,J.C. (1997). LINCS: A linear constraint solver for molecular simulations. J Comp Chem 18**,** 1463-1472.

Bjelkmar,P., Larsson,P., Cuendet,M.A., Hess,B., and Lindahl,E. (2010). Implementation of the CHARMM Force Field in GROMACS: Analysis of Protein Stability Effects from Correction Maps, Virtual Interaction Sites, and Water Models. J Chem Theory Comput 6**,** 459-466.

Bussi,G., Donadio,D., and Parinelli,M. (2007). Canonical sampling through velocity rescaling. J. Chem. Phys. 126**,** 014101.

Jorgensen,W.L., Chandrasekhar,J., Madura,J.D., Impey,R.W., and Klein,M.L. (1983). Comparison of simple potential functions for simulating liquid water. J Chem Phys 79**,** 926.

Lomize,M.A., Lomize,A.L., Pogozheva,I.D., and Mosberg,H.I. (2006). OPM: Orientations of proteins in membranes database. Bioinformatics 22**,** 623-625.

Pronk,S., Pall,S., Schulz,R., Larsson,P., Bjelkmar,P., Apostolov,R., Shirts,M.R., Smith,J.C., Kasson,P.M., van der,S.D., Hess,B., and Lindahl,E. (2013). GROMACS 4.5: a high-throughput and highly parallel open source molecular simulation toolkit. Bioinformatics 29**,** 845-854.